Article

Spectroscopic confirmation of four metal-poor galaxies at z = 10.3–13.2

A list of authors and their affiliations appears at the end of the paper

Finding and characterizing the first galaxies that illuminated the early universe at cosmic dawn is pivotal to understand the physical conditions and the processes that led to the formation of the first stars. In the first few months of operations, imaging from the James Webb Space Telescope (JWST) has been used to identify tens of candidates of galaxies at redshift (z) greater than 10, less than 450 million years after the Big Bang. However, none of such candidates has yet been confirmed spectroscopically, leaving open the possibility that they are actually low-redshift interlopers. Here we present spectroscopic confirmation and analysis of four galaxies unambiguously detected at redshift $10.3 \leq z \leq 13.2$, previously selected from JWST Near Infrared Camera imaging. The spectra reveal that these primeval galaxies are metal poor, have masses on the order of about 10^7–10^8 solar masses and young ages. The damping wings that shape the continuum close to the Lyman edge provide constraints on the neutral hydrogen fraction of the intergalactic medium from normal star-forming galaxies. These findings demonstrate the rapid emergence of the first generations of galaxies at cosmic dawn.

The opening act of galaxy formation in the first billion years after the Big Bang set in motion the physics of galaxy formation and evolution that shapes galaxy properties across cosmic time. Galaxies forming at these times may be the seeds of the much more massive and mature galaxies in the local universe. Theoretical models and cosmological simulations differ greatly in their predictions of the physical properties and abundance of the first galaxies. The theoretical pictures depend strongly on assumptions about the physical processes at play in the early universe, such as: gas cooling and fragmentation in primordial clouds; the feedback effects from first stars and supernova explosions that subsequently enrich the surrounding medium; and early merging, assembly and accretion histories of galaxies[1–7]. The abundance and mass distribution of the first galaxies are also tightly connected to early structure formation. Therefore, the detection and characterization of these early galaxies is key to test different models and theories.

High-redshift galaxies often have distinctive spectra in the ultraviolet (UV), in which the blue spectrum produced by hot massive stars is abruptly cut off below the Lyman limit at 912 Å (rest frame) by the absorption of the light by neutral hydrogen in stellar atmospheres, interstellar gas and the intergalactic medium (IGM). At the highest redshifts ($z \gtrsim 6$), the intergalactic neutral hydrogen leads to almost complete absorption at wavelengths below Lyman α (Lyα) at 1,216 Å. Observationally, this translates to a 'dropout', that is, a lack of detection in bands bluewards of $(1 + z) \times 1,216$ Å but flux redwards of the same wavelength[8–10]. However, galaxies with peculiar properties may mimic high-redshift galaxies (for example, a combination of dust reddening and nebular lines or contribution by an active galactic nucleus as in ref. [11]). Therefore, spectroscopic observations are the only method to determine accurate redshifts, either via the detection of the (redshifted) nebular lines[12], or via the unambiguous detection of the sharp continuum cut-off at $(1 + z) \times 1,216$ Å. The highest-redshift, spectroscopically confirmed galaxy before these observations is that of GN-z11 at $z = 10.957$ (refs. [13,14]).

Identification and spectroscopic characterization of galaxies in the early universe is one of the primary goals for which the James Webb Space Telescope (JWST) was designed. The first few months of JWST imaging have already yielded a large number of candidate galaxies at $z > 10$ (refs. [15–22]). However, the redshift estimates of these candidates have so far been based on their broad-band spectral energy distributions (SEDs), and it cannot be ruled out that such candidates are actually

✉e-mail: e.curtis-lake@herts.ac.uk; stefano.carniani@sns.it
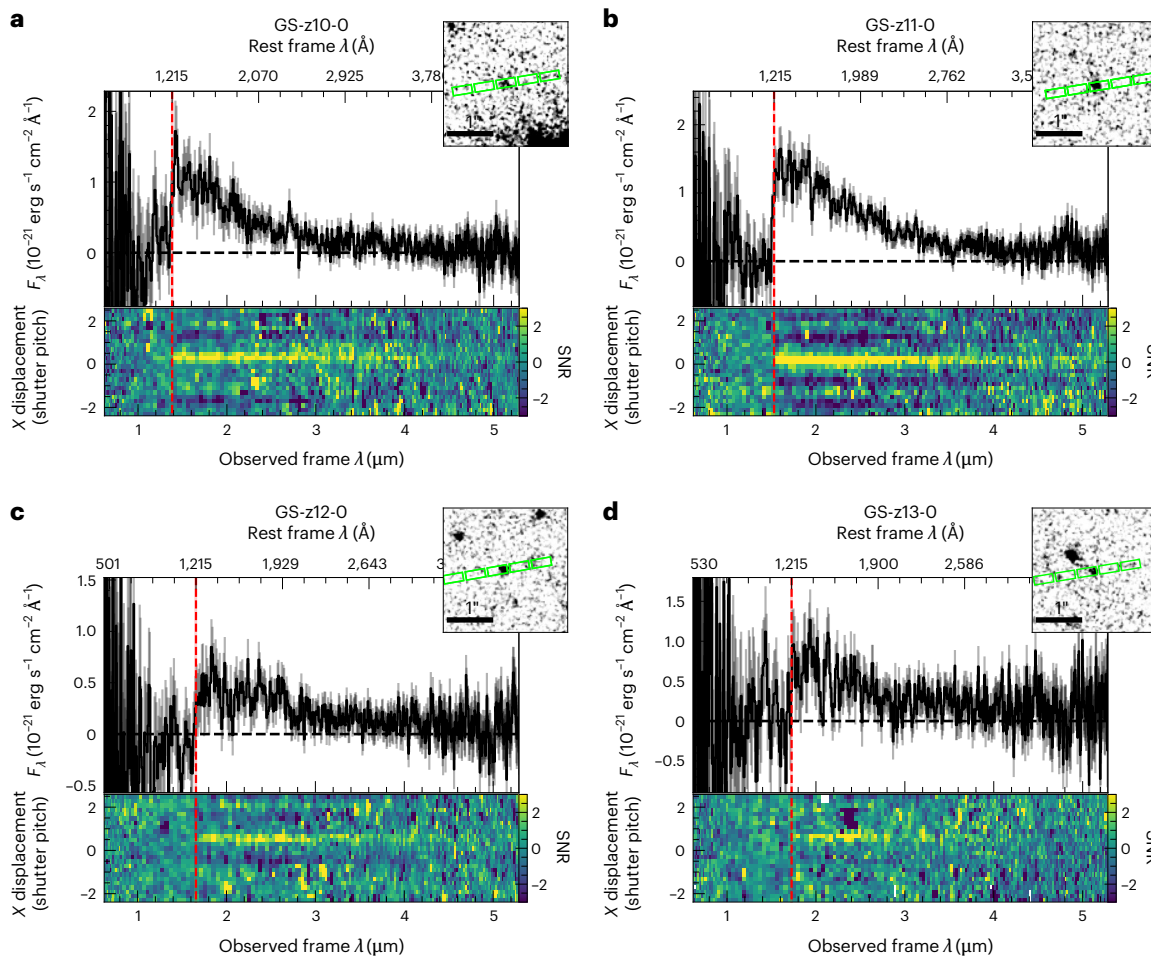
Fig. 1 | Spectra of the four z > 10 galaxies targeted for the first deep spectroscopic pointing of the JADES survey. a–d, NIRSpec prism $R \approx 100$ spectra for JADES-GS-z10-0 (**a**), JADES-GS-z11-0 (**b**), JADES-GS-z12-0 (**c**) and JADES-GS-z13-0 (**d**). For each galaxy, we show the 1D spectrum and associated 1σ uncertainties (which are derived from standard error propagation through the reduction pipeline). F_λ is the spectral flux density per unit wavelength. In the bottom panels, we show the 2D SNR plots. The 2D plots are binned over four pixels in the wavelength direction to better show the contrast across the break. The top-right inset panels show the NIRCam F444W filter images with the three nodding positions of the NIRSpec microshutter three-slitlet array aperture shown in green. The red dashed line shows 1,215.67 Å at the observed redshift $z_{1,216}$.

lower-redshift galaxies[11], especially in regions where accompanying Hubble Space Telescope (HST) imaging is relatively shallow. With the large number of $z > 10$ candidates identified in the first months of JWST science observations from Near Infrared Camera (NIRCam) photometry, some initial findings suggest very little evolution of the UV luminosity function above $z > 10$ (refs. [18,23]; although this is not seen in ref. [15]). This would require early galaxies to display different physics, for example, a stellar initial mass function more top heavy than in lower-redshift galaxies[18]. Yet ref. [24] illustrates how large a difference in UV luminosity density evolution is measured when considering only the robust candidates. This demonstrates the firm need for spectroscopic observations to follow up photometric candidates. In addition, spectra provide us with constraints on the stellar and gas properties of the objects beyond what photometry can provide.

In this Article, we report deep spectroscopic observations with the Near Infrared Spectrograph (NIRSpec)[25] on JWST, which provide confirmation of four candidates at $z > 10$ and extensive characterization of their physical properties. These candidates were photometrically identified as part of the JWST Advanced Deep Extragalactic Survey (JADES), a joint guaranteed time project of the NIRCam and NIRSpec instrument teams. The identification and photometric study of these candidates, based on HST and NIRCam data[26], is described in a companion paper[27]. We specifically focus here on a pointing in the Hubble

Ultra Deep Field (in the GOODS-South area), in which we have taken multi-object spectroscopy of 253 galaxies observed simultaneously with NIRSpec's configurable array of microshutters. We report here on observations taken with the prism spectral configuration (spectral range 0.6–5.3 μm, resolving power $R \approx 100$) with exposure times ranging from 9.3 h to 28 h (see Methods for details on the observing strategy).

The JADES spectroscopic observations reach an unprecedented sensitivity of 28.4 magnitudes (AB) at 5σ per resolution element on the continuum at 2.5 μm. We note that the NIRSpec prism is extremely well suited for the redshift confirmation of high-redshift candidates, with low spectral resolution and high sensitivity at short wavelengths where we are searching for a spectral break (around 1–2 μm), and higher resolution in the 3–5 μm region, where we are searching for narrow spectral lines.

The focus of this paper is on four of these spectroscopic targets. Two of these are $z > 12$ galaxy candidates selected from NIRCam imaging[27], based on a clear lack of F150W flux. Two others are $z > 10$ candidates based on their HST infrared photometry. We defer to a future publication to describe the other targets in this deep pointing. All candidates are faint, with F200W magnitudes fainter than 28 (AB), and hence entirely out of reach for any spectroscopic facility before JWST. More details on the selection and photometric properties of these candidates are provided in the companion paper[27].

Table 1 | Parameters of the four z>10 galaxies

JADES ID	GS-z10-0	GS-z11-0	GS-z12-0	GS-z13-0
Full name	JADES-GS+53.15884−27.77349	JADES-GS+53.16476−27.77463	JADES-GS+53.16634−27.82156	JADES-GS+53.14988−27.77650
Exposure time (s)	67,225.6	100,838.0	67,225.6	33,612.8
$z_{1,216}$ [a]	$10.38^{+0.07}_{-0.06}$	$11.58^{+0.05}_{-0.05}$	$12.63^{+0.24}_{-0.08}$	$13.20^{+0.04}_{-0.07}$
z_{HI} [b]	$10.37^{+0.03}_{+0.02}$	$11.48^{+0.03}_{-0.08}$	$12.6^{+0.04}_{-0.05}$	$13.17^{+0.16}_{-0.15}$
EW(C III]) (Å) 2σ	<13.8	<5.9	<12.4	<15.2
EW(He II) (Å) 2σ	<14.8	<6.0	<13.5	<15.4
EW([O II]) (Å) 2σ	<28.1	<9.1	<16.6	<16.8
2σ break strength	>2.04	>6.85	>2.48	>2.79
M_{UV}	−18.61 ± 0.10	−19.34 ± 0.05	−18.23 ± 0.16	−18.73 ± 0.06 [c]
β	−2.49 ± 0.22	−2.18 ± 0.09	−1.84 ± 0.19	−2.37 ± 0.12 [c]
$\log(M/M_\odot)$	$7.58^{+0.19}_{-0.20}$	$8.67^{+0.08}_{-0.13}$	$7.64^{+0.66}_{-0.39}$	$7.95^{+0.19}_{-0.29}$
Ψ (M yr^{-1}) [d]	$1.1^{+0.19}_{-0.16}$	$2.2^{+0.28}_{-0.22}$	$1.8^{+0.54}_{-0.43}$	$1.36^{+0.31}_{-0.23}$
$\log[t \, (yr)]$ [e]	$7.54^{+0.25}_{-0.20}$	$8.35^{+0.08}_{-0.17}$	$7.36^{+0.75}_{-0.59}$	$7.84^{+0.23}_{-0.36}$
$\log(Z/Z_\odot)$ [f]	$-1.91^{+0.25}_{-0.20}$	$-1.87^{+0.28}_{-0.18}$	$-1.44^{+0.23}_{-0.22}$	$-1.69^{+0.28}_{-0.31}$
$\hat{\tau}_V$ [g]	$0.05^{+0.03}_{-0.02}$	$0.18^{+0.06}_{-0.06}$	$0.17^{+0.20}_{-0.09}$	$0.10^{+0.08}_{-0.05}$
ξ_{ion} [h]	$25.46^{+0.07}_{-0.07}$	$25.43^{+0.06}_{-0.06}$	$25.72^{+0.16}_{-0.19}$	$25.47^{+0.10}_{-0.09}$

Exposure times, redshifts (derived both from assuming the spectral break is at exactly 1,215.67 Å and accounting for the damping wing from a fully neutral IGM), 2σ upper limits on emission-line EWs (rest frame) for the C III] $\lambda\lambda$1,907, 1,909, He II λ1,640 and [O II] $\lambda\lambda$3,726, 3,729 lines, 2σ lower limits on the strength of the observed spectral breaks (measurements described in 'Empirical measurements' in Methods), UV absolute magnitude, M_{uv}, and UV slope, β (measured directly from the spectra; see 'M_{UV} and UV slopes' in Methods) and BEAGLE-derived physical properties for the four objects. For the BEAGLE-derived properties, we report posterior medians and limits in the 1σ credible region. [a]The redshift based on the spectral break being at 1,215.67 Å. [b]The redshift accounting for a fully neutral IGM (x_{HI}=1) following the method outlined in 'Balmer break index' in Methods. [c]For JADES-GS-z13-0, we report β and M_{uv} derived from the BEAGLE fitting, as we know this object to be on the edge of the shutter, and hence incorporate NIRCam photometry in the fitting to this one object to account for slit losses (see 'BEAGLE SED fitting' in Methods). [d]Ψ is the star formation rate. [e]t is the age of the oldest stars, or maximum stellar age. [f]Z is the metallicity. [g]$\hat{\tau}_V$ is the effective V-band attenuation optical depth. [h]The production rate of H-ionizing photons per unit monochromatic UV luminosity.

In Fig. 1, we show the one-dimensional (1D) and two-dimensional (2D) spectra of these four galaxies. All show a clear detection of a blue continuum that drops off sharply in a manner consistent with a $z > 10$ Lyman dropout. Specifically, in Fig. 1, we show the redshift derived from the position of the spectral break, taken to be at the wavelength of Lyα at 1,215.67 Å. These redshifts are reported in Table 1 and were derived with full spectral fitting over the entire redshift range, with each object consistently showing peaks in the posterior probability distribution only at high redshifts. We note that both the spectra and the photometry from ref. [27] agree on the wavelength of the break.

We tested whether the observed breaks might be produced by the Balmer (or 4,000 Å) break in the stellar continuum associated with evolved stellar populations in galaxies at $z \approx 3$, and we show that this possibility is excluded with high confidence (see Methods and model Balmer break strength in Extended Data Fig. 1). Other, more extreme, low-redshift solutions are still able to explain the photometry of our objects. In particular, fitting with active-galactic-nuclei narrow-line emission (not often included when performing photometric redshifts) provides intermediate redshift solutions at $z \approx 3$–3.5, as shown in Methods. In these solutions, the strong photometric break is produced by strong line emission in certain filters. We can firmly rule out these low-redshift solutions with our spectra, which demonstrates that the photometric fluxes arise from continuum emission, rather than strong emission lines with weak underlying continuum. Although this low-redshift solution may appear extreme, we emphasize that the JWST is pushing into a new regime of exploration, where yet-unexplored families of low-redshift contaminants may be uncovered. A recent discovery of a triply imaged point source shows a similarly extreme possible SED explained by strong line emission at a photometric redshift of $z_{phot} = 7.7$ (ref. [28]).

One of the galaxies, JADES-GS-z11-0, has been debated in the literature. It was first identified in ref. [29] as a potential $z \approx 10$ galaxy. In the 2012 Hubble Ultra Deep Field survey[30,31], deep Hubble imaging revealed that the object drops out in JH_{140} band imaging. This left two possibilities: either the source was at very high redshift ($z \approx 11.9$ (ref. [30])), or was low redshift, with a high-equivalent-width (EW) emission line producing the flux in the Hubble H_{160} image. In fact, ref. [32] found indication of a possible emission line in spectroscopic follow-up supporting the latter explanation. We do not confirm this line emission in our NIRSpec spectroscopy, and the NIRCam imaging present in ref. [27] shows that the continuum emission extends to longer wavelengths, which is consistent with the spectrum shown here (see also ref. [23]). Therefore, this galaxy is indeed at high redshift, and not a low-redshift contaminant.

The continua appear mostly featureless, with the possible exceptions of JADES-GS-z10-0, which shows a tentative emission line at about 1.44 μm, which may indicate Lyα emission, and JADES-GS-z12-0, which shows another tentative feature at about 5.23 μm, which could be interpreted as [Ne III] λ3,869 emission at $z = 12.52$. However, both features are only marginally detected, and we are still assessing whether these very faint and localized features are astrophysical. They will be assessed and explored more in detail in forthcoming papers and not discussed further here. Remarkably, the lack of strong line detections turns out to be what makes these spectra particularly interesting as it provides vital information over and above the spectroscopic redshift determination, and what could be derived from photometry alone[27].

Leaving aside the above two features, we report the 2σ upper limits on the EWs of He II λ1,640, C III] $\lambda\lambda$1,907, 1,909 and [O II] $\lambda\lambda$3,726, 3,729 in Table 1 (see 'Limits on possible emission lines' in Methods for details of the measurements and Extended Data Table 1 for further limiting fluxes). These lines are important as C III] $\lambda\lambda$1,907, 1,909 is

often the strongest line in the rest-frame UV of low-metallicity galaxies (for example, ref. [33]) and strong He II $\lambda1,640$ is expected in galaxies of near-zero metallicity. Nearby metal-poor galaxies (metallicity $Z/Z_\odot \lesssim 0.1$, where $Z_\odot$ is solar metallicity) show EWs of C III] $\lambda\lambda1,907$, 1,909 spanning about 6–16 Å (refs. [33,34]), meaning our limits are constraining only in the upper region of this range. The limits on EW(He II $\lambda1,640$) are above the actually measured EWs in these studies, and comparable to or higher than the majority of objects in the Multi Unit Spectroscopic Explorer-selected sample of ref. [35] spanning $2 \lesssim z \lesssim 4$. However, JADES-GS-z10-0 and JADES-GS-z11-0 still show strong limits on the EW of [O II] $\lambda\lambda3,726$, 3,729. These limits are constraining, showing that [O II] $\lambda\lambda3,726$, 3,729 is weak compared with the average EWs measured in $z \approx 3$ galaxies (~80 Å at 10^9 solar masses)[36].

We can gain further insight into the physical properties of these galaxies through spectral fitting with the Bayesian Analysis of Galaxy SEDs (BEAGLE)[37] tool with set-up described in Extended Data Table 2, adopting a constant star formation history to probe the young stellar populations within them (see 'BEAGLE SED fitting' in Methods for more details). These fits are illustrated in Extended Data Figs. 2–5. We find low metallicities, with two galaxies, JADES-GS-z10-0 and JADES-GS-z11-0, showing strong constraints of just a few per cent of solar. At higher metallicities, we would expect a significant detection of [O II] $\lambda\lambda3,726$, 3,729. For the two highest-redshift galaxies, a low metallicity is still preferred, but the constraints are less strong due to [O II] $\lambda\lambda3,726$, 3,729 being very close to the edge of the observable wavelength coverage of NIRSpec, where the signal-to-noise ratio (SNR) is low, as well as lower SNR in regions of the rest-frame UV lines.

The measured star formation rates are moderate, at just a few solar masses a year. We caution that total star formation rates and stellar masses require slit-loss corrections, which can be best derived from NIRCam photometry if the objects are extended, or on the edge of the shutter. Still, we find excellent agreement in absolute magnitude and UV slope compared with those derived from NIRCam photometry alone[27] for the two galaxies well centred within the microshutters (GS-z10-0 and GS-z11-0). The fitted parameters are given in Table 1.

It is of interest to investigate whether the lack of detectable line emission requires a large escape fraction of ionizing photons and find no strong dependence of the physical properties, nor strong constraints on the escape fraction. We do note, however, that JADES-GS-z11-0 has a solution with low ages and high escape fraction with marginally higher metallicity, though the upper 1σ limit is still about 5% solar metallicity (Extended Data Table 3). In fact, at these extremely low metallicities, the rest-frame UV emission lines might be substantially weaker than those sometimes found in lower-redshift samples with somewhat higher metallicities around about 10% solar. Another important factor is the age of the stellar populations, as strong UV emission lines have primarily been observed in galaxies with UV light dominated by very young stellar populations ($\lesssim10$ million years[33]).

Two objects, JADES-GS-z11-0 and JADES-GS-z12-0, do indicate moderate levels of dust, albeit with large uncertainties (with effective V-band absorption optical depth, $\tau_v = 0.18^{+0.06}_{-0.06}$ and $\tau_v = 0.2^{+0.16}_{-0.09}$, respectively). Such high optical depth due to dust in such low-metallicity systems would be physically hard to explain unless a low dust-to-gas ratio were integrated over large H I column densities. However, we note that some recent models expect substantial dust production by the first generations of stars[3,38]. When fit without any dust, JADES-GS-z11-0 required a higher metallicity (up to 40% solar at 1σ), whereas the JADES-GS-z12-0 data yielded similar parameter constraints to those reported in Table 1.

The spectra do not provide strong constraints redwards of the Balmer break, the longest rest-frame wavelength probed being about 3,660–4,350 Å. We see no evidence for strong Balmer breaks in these objects, but the SNR in this region of the spectra is low. Correspondingly, the constraints on stellar age and stellar mass (sensitive to the
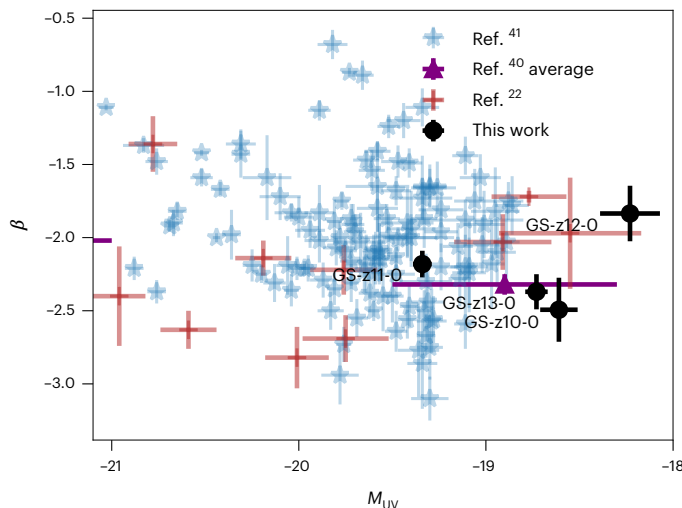

Fig. 2 | UV slope versus magnitude for the four $z > 10$ galaxies. Measured UV slope, β, as a function of absolute magnitude at 1,500 Å, M_{UV}, measured as described in 'M_{UV} and UV slopes' in Methods. These are compared with the measurements from photometrically selected high-redshift candidates. Specifically, the average β measured from objects spanning $z \approx 8$–15 at similar M_{UV} from ref. [40], as well as a sample from ref. [22] spanning $z \approx 9$–16 and the sample presented in ref. [41] (itself collated from the samples of refs. [21],[64] and spanning $z \approx 7$–11). In all cases, the error bars show the 1σ measurement uncertainties, except in the case of the point showing the average UV slope from ref. [40]. For the ref. [40] datapoint, the point shows the inverse-variance weighted mean and standard error of β, plotted against the median M_{UV} of their sample of 41 galaxies in their lower luminosity bin. The error bar for M_{UV} is σ_{MAD} (where $\sigma_{MAD} = 1.483 \times MAD$ and MAD is the median absolute deviation) of the individual M_{UV} values.

Balmer break strength) are broad. The ages range from about 5 Myr to 230 Myr, and stellar masses range from about 2×10^6 $M_\odot$ to 460×10^6 $M_\odot$, although the constraints on these parameters are weak, and highly sensitive to the prior regarding the onset of star formation. The associated production rates of hydrogen-ionizing photons per unit monochromatic UV luminosity, ξ_{ion}, are similar to those measured in extreme star-forming regions in low-redshift, metal-poor galaxies[39].

We show the measured UV slopes (β) versus absolute magnitude at 1,500 Å (M_{uv}) in Fig. 2. We compare to other JWST-selected high-redshift candidate samples spanning photometric redshifts $z \approx 7$–16 (refs. [22,40,41]). Our measured slopes at such faint M_{uv} magnitudes are comparable to the other literature samples, suggesting little evolution at these epochs. Very blue UV slopes are used to search for extreme stellar populations at the earliest times[42]. In this case, we find extreme stellar populations but the presence of any nebular recombination continuum will redden the UV slopes[41]. Indeed, we expect strong nebular continuum emission in low-metallicity galaxies unless a large fraction of their ionizing photons escape into the IGM.

If ionizing radiation does escape from galaxies, it will reionize neutral hydrogen in the surrounding gas. We find that the breaks in the spectra presented in Fig. 1 are less abrupt than those seen in galaxies at lower redshifts in our spectroscopic dataset, and are consistent with a softening of the break by the Lyα damping wing caused by a largely neutral IGM, suggesting that these galaxies are yet to ionize large bubbles in their near vicinity. The redshift is sensitive to the existence and form of this damping wing, and we report the best-fit redshift for a fully neutral IGM ($x_{HI} = 1$, where x_{HI} is the fraction of neutral hydrogen) in Table 1. For the object with the highest SNR in the Lyα break region (JADES-GS-z11-0), we investigate the constraints we can place on the neutral hydrogen fraction by first fixing the best-fit model for the stellar population. We then run BEAGLE varying only z and x_{HI}. The resulting fit to the spectral break and the derived constraints are shown in Fig. 3. The
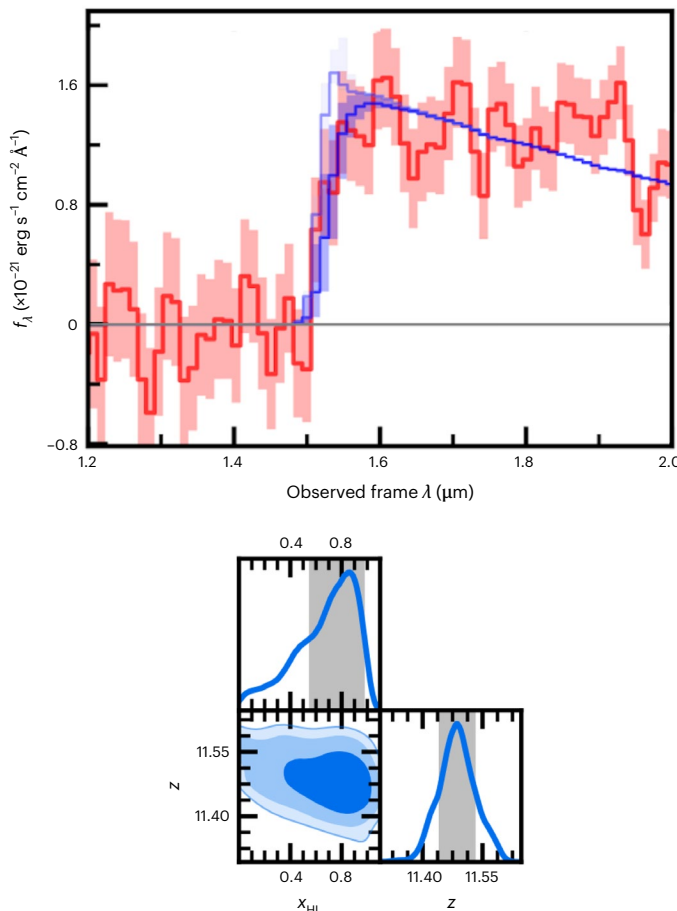
Fig. 3 | Spectral break fit region and the derived constraints on neutral hydrogen in the IGM for JADES-GS-z11-0. Top: BEAGLE fit to the spectral break region of JADES-GS-z11-0, while varying the fraction of neutral hydrogen in the IGM, x_{HI}. The red line and shaded region show the extracted spectrum and per-pixel 1σ uncertainties and the darker blue line and shaded region shows the range and median of the fitted models, respectively. The lighter blue line shows the underlying intrinsic spectrum before application of the damping wing. Bottom: the 2D constraints on redshift and x_{HI}, which were varied in the fit while keeping all other physical properties constant (see text for details). The dark, medium and light blue contours show the extents of the 1, 2 and 3σ credible regions of the joint posterior probability, respectively, while the top and right panel show the 1D posterior probability distribution for x_{HI} and redshift, respectively, with the 1σ credible region shaded in grey. For this test, we use a spectral extraction over 3 pixels that maximizes the SNR in the region of the break. The shape of the damping wing is not sensitive to wavelength-dependent slit losses introduced by such a small extraction box as the wing extends over just tens of pixels.

2D posterior probability distribution function reported in the bottom panel indicates that the constraints on x_{HI} are fairly weak, suggesting $x_{HI} > 0.5$ from the 1σ credible interval, although this is sensitive to exact redshift of the source (for example, Extended Data Fig. 6). However, these spectra demonstrate that x_{HI} can be constrained from JWST R100 spectra at slightly lower redshifts from 'normal' star-forming galaxies.

So far, the only constraints on the evolution of x_{HI} from damping wings is in luminous quasars at $6 < z < 7.5$. Damping wings are rarely observed at $z < 7$, but become more common in the small sample of known $z > 7$ quasars, consistent with $x_{HI} \approx 0.5$ at $z = 7.3$ (ref. [43]). While star-forming galaxies are less luminous than quasars, they have several advantages in being plentiful at $z = 7–9$ and providing an independent test of neutrality at higher redshifts. Finally, galaxies do not exhibit broad Lyα and N v λ1,240 emission, which may simplify the damping-wing modelling[44].

We conclude by emphasizing that the results reported here represent a milestone for the JWST mission, pushing the spectroscopic frontier to a markedly earlier epoch of galaxy formation. In addition to providing clear detections of Lyman dropouts as high as $z = 13.2$, these JADES observations also show the power of spectroscopy to probe the physics of these galaxies, revealing low metallicities through the lack of emission lines, as well as the state of the surrounding IGM. This is just a starting point for the mission. JADES and other programmes have extensive amounts of spectroscopy approved for JWST-detected high-redshift candidates.

Methods

NIRSpec observations and data reduction

The NIRSpec observations presented here are part of guaranteed time observation (GTO) programme ID 1210 (principal investigator: Lützgendorf) and were obtained between 22 and 25 October 2022. The programme used a three-point nod pattern for background subtraction, as well as three small dithers with microshutter array (MSA) reconfigurations to improve spatial sampling, increase sensitivity and flux accuracy, mitigate the impact of the detector gaps and aid removal of cosmic rays.

Each dither pointing included four sequences of three nodded exposures each to build up the SNR. Observations were carried out by using the disperser-filter combination PRISM/CLEAR, which covers the wavelength range between 0.6 µm and 5.3 µm and provides spectra with a spectral power of $R \approx 100$ (ref. [25]). Each PRISM/CLEAR set-up had two integrations of 19 groups, resulting in an exposure time of 8,403.2 s for each sequence and of 33,612 s for each dither pointing.

A total of 253 galaxies were observed over the three dither pointings. As the non-functioning shutters and rigid grid of the MSA prevents some slit locations from being used, some galaxies were not observed on all three pointings. More specifically, among the four sources presented in this paper, JADES-GS-z11-0 was observed in all three MSA dither pointings, JADES-GS-z10-0 and JADES-GS-z12-0 were present in two dither pointings, whereas JADES-GS-z13-0 was only observed in one dither pointing. The different resulting exposure times for each target are reported in Table 1.

Flux-calibrated 2D spectra and 1D spectral extractions have been produced using pipelines developed by the European Space Agency NIRSpec Science Operations Team (SOT) and the NIRSpec GTO Team. We briefly outline here the main steps, while a more detailed description will be presented in a forthcoming NIRSpec/GTO collaboration paper. Most of the processing steps in the pipelines adopt the same algorithms as included in the official Space Telescope Science Institute (STScI) pipeline used to generate the Barbara A. Mikulski Archive for Space Telescopes (MAST) archive products (see Fig. 11 and section 4.3 of ref. [45]). Initially, we processed the multi-object spectroscopy raw data (that is, level 1a data from the MAST archive) with the ramp-to-slope pipeline, which estimates the count rate per pixel by using all unsaturated groups in the ramp. Ramp jumps due to cosmic rays are detected and rejected on the basis of the slope of the individual ramps. The ramp-to-slope pipeline also includes the following steps: saturation detection and flagging, master bias subtraction, reference pixel subtraction, linearity correction, dark subtraction, snowball artefact detection and correction, and count-rate estimation (for more details see refs. [46–48]). All the count-rate images were then processed using a data reduction pipeline including European Space Agency NIRSpec SOT codes and NIRSpec GTO algorithms. The pipeline has 11 main steps: (1) identification of non-target galaxies intercepting the open shutters; (2) pixel-level background subtraction by combining the three nod exposures (excluding nods contaminated by non-target sources); (3) extraction of subimages containing the spectral trace of each target and wavelength and spatial coordinate assignments to each pixel in the 2D maps; (4) pixel-to-pixel flat-field correction; (5) spectrograph optics and dispersers correction; (6) absolute flux calibration; (7) slit-losses

correction; (8) rectification of the spectral trace; (9) extraction of 1D spectra; (10) combination of 1D spectra generated from each integration, nod and pointing; (11) combination of 2D maps. The data processing workflow thus returns both a combined 1D and 2D spectrum for each target. We stress, however, that the combined 1D spectra are not extracted from the combined 2D maps, but are the result of a weighted average of 1D spectra from all integrations. This process allowed us to mask the bad pixels indicated on the quality flags and to reject outlier pixels. Finally, we adopted an irregular wavelength grid for the 1D and 2D spectra to avoid oversampling of the line spread function at short wavelengths ($\lambda \approx 1\,\mu m$).

Given the compact size of our $z > 10$ targets, we computed and applied slit-loss corrections, modelling galaxies as point-like sources, but taking into account the relative intra-shutter position of each source (each microshutter has an illuminated area of $0.2'' \times 0.46''$). For each target, we extracted the 1D spectra from two different apertures. One aperture was as large as the shutter size to recover all emission of the galaxy, while the second extraction was performed in an aperture of 3-pixels height (with NIRSpec spatial pixel scale of $0.1''$ per pixel) to maximize the SNR of the final spectra.

For most uses of the extraction performed on a 3-pixel aperture, the measurements are performed over small wavelength ranges and further corrections for losses due to the smaller extraction box are not required. In the case of full spectral fitting, we use the extraction over the 5-pixel aperture with one exception, JADES-GS-z13-0. In this case, we mitigate the wavelength-dependent losses with simultaneous fitting to photometry (see 'BEAGLE SED fitting').

Empirical measurements

The central aspects of the astrophysical analysis of the spectra has been presented in the main part of the paper. Here we explore a few more issues that bolster the fidelity and robustness of our analysis.

Balmer break index. While the observed spectral breaks in the four objects presented here are fully consistent with expectations for high-redshift galaxies, it is important to test the possibility that the observed breaks may be Balmer breaks at lower redshift. We test this using empirical spectral indices. We adapt the classical Balmer break index definition[49] and define the break amplitude as the ratio of f_λ (the spectral flux density per unit wavelength) in the rest-frame range 3,751–4,198 Å to that in the range 3,145–3,563 Å. This definition expands the spectral windows to include more spectral pixels (15–19 depending on redshift) and increase the SNR on the index. These measurements are taken from spectra extracted from 3 pixels, maximizing the SNR. The effect of wavelength-dependent extraction losses should be minimal for this measurement. When the lower spectral range yields a negative flux, we adopt the 2σ upper flux limit instead. In addition, to account for the noisy measurement of the (physically) positive-definite flux in the longer-wavelength band, we subtract 1σ from the measured flux. This is a conservative upper limit, which we quote as a 2σ upper limit in Table 1.

In Extended Data Fig. 1, we show the evolution of the modified Balmer break index with age for single stellar population models at four different metallicities from $0.01\,Z_\odot$ to $1\,Z_\odot$. The maximum value reached within 10 Gyr is less than 2.0. We report 2σ lower limits on the value of this index for each of our four targets in Table 1. The smallest measured break strength is measured for GS-z10-0, with a 2σ lower limit of 2.04, which is higher than the maximum reached by the single stellar populations. Again, this suggests that the Balmer break solution is unlikely, although by a smaller margin than for the other three targets.

We note that incorrect background subtraction due to contamination of background shutters by neighbouring galaxies or the source itself can lead to a biased measurement of the break strength. We are careful with the reduction to exclude any contaminated shutters in the background estimate, as described in 'NIRSpec observations and data

reduction', and so do not expect these measurements to be affected in this way.

Limits on possible emission lines. Apart from the possible detections of Lyα in JADES-GS-z10-0 and [Ne III] $\lambda3,869$ in JADES-GS-z12-0 (which we will assess in future work), visual inspection of the 1D and 2D spectra did not show the presence of any emission lines above the level of the noise in any of the four targets. We derive upper limits to emission-line fluxes and EWs using the error spectrum output from the data reduction pipeline for the optimized SNR spectra extracted over 3 pixels. Our reduced spectra have an irregular wavelength grid, and we estimate that the line spread function of these PRISM spectra results in unresolved emission lines with full-width at half-maximum of approximately two to three spectral pixels. Thus, to calculate emission-line limits, for the three spectral pixels centred on the expected centroid of the emission line at the calculated redshift, we sum the pixel errors in quadrature and multiply the result by the wavelength interval between pixels. This results in 1σ upper limits on line fluxes, which we convert into EW limits by fitting a simple polynomial to the continuum of each object to get the level on the continuum and associated uncertainty. Table 1 reports 2σ upper limits on the EWs of He II $\lambda1,640$, C III] $\lambda\lambda1,907$, 1,909 and [O II] $\lambda\lambda3,726$, 3,729 while the full set of limits on rest-frame UV emission lines is given in Extended Data Table 1.

$M_{\rm UV}$ and UV slopes. The UV slope, β, was determined directly from the 1D extracted spectra. We performed a least-squares fit to the gradient in the $\ln(\lambda)$:$\ln(f_\lambda)$ space, with the errors on $\ln(f_\lambda)$ taken to be $\ln(f_\lambda + \sigma) - \ln(f_\lambda)$ for each extracted spectral pixel (where σ is the noise). For all objects, we fit the β slope over the rest-frame wavelength range 1,250–2,600 Å, following ref. [50] (fitting to the entire wavelength range, as absorption features avoided with the spectral windows of ref. [50] will not substantially affect the measurement at this level of SNR and resolution), with the exception of JADES-GS-z10-0 where we used a slightly smaller range of 1,500–2,600 Å to avoid the possible Lyα emission and damping wing. These results were also consistent with those from fitting a power law to $f_\lambda \propto \lambda - \beta$ in linear wavelength space, weighting each point by $1/\sigma^2$.

We determined the absolute magnitude in the rest-frame UV ($M_{\rm UV}$) around $\lambda_{\rm rest} = 1,500$ Å by measuring the average flux density per unit frequency interval (f_ν) from the extracted spectra over the rest-frame wavelength range 1,400–1,600 Å, and accounting for luminosity distance. The errors on each individual pixel flux density were combined in quadrature to derive the uncertainty in β.

We note that $M_{\rm UV}$ measured from the spectrum alone is somewhat fainter and the β somewhat redder for JADES-GS-z12-0 than that measured from NIRCam data in the companion paper[27]. We attribute this to residual slit losses missed by our standard correction, as this object is quite close to the edge of the shutter. This highlights the importance of the complementarity between NIRSpec spectroscopy and NIRCam photometry. The difference is starker for JADES-GS-z13-0, which is very close to the edge of the shutter, and for which we report instead $M_{\rm UV}$ and β derived from SED modelling including the NIRCam photometry (see 'BEAGLE SED fitting'). The comparison with the measurements in ref. [27] shows good agreement for JADES-GS-z10-0 and JADES-GS-z11-0, which validates the spectroscopic flux calibration in the case where the adoption of point-source path losses is a good approximation.

BEAGLE SED fitting

We perform full spectral fitting to the R100 spectra using the BEAGLE code[37]. In general, firm constraints on metallicities (both nebular and stellar) and gas parameters require the spectroscopic detection of emission and absorption lines, while constraints on total stellar masses and star formation rates generally require NIRCam photometry, as NIRSpec MSA spectra are so prone to slit losses. As these objects are so small (with half light radii 50–165 pc, with on-sky sizes of 0.015–0.04″ (ref. [27])), we use pre-calculated point-source slit-loss corrections. Therefore, in

this paper, we present an entirely independent analysis to that in ref. [27], both in datasets used (except for the fits to JADES-GS-z13-0 where we employ the NIRCam photometry, see later in this section for details), in SED codes and parameterizations. We comment on the consistency between the two analyses throughout this section.

This requires modelling of the wavelength-dependent line spread function. We fit Gaussian profiles to emission lines in R100 spectra taken within this deep pointing and compare their widths as a function of wavelength to the dispersion curves provided by STScI (https://jwst-docs.stsci.edu/jwst-near-infrared-spectrograph/nirspec-instrumentation/nirspec-dispersers-and-filters). We find that the supplied dispersion curves multiplied by a factor of 0.7 provide a reasonable representation of the measured wavelength-dependent line spread function.

We use spectra extracted over the full microshutter aperture to minimize the effects of wavelength-dependent losses, as the size of the shutter is more than twice the width of the point spread function at 5 μm. JADES-GS-z13-0, however, is just at the edge of the shutter and the 2D spectrum shows that it is clearly truncated. Therefore, to provide information of the aperture losses for this target, we use a 3-pixel extraction box to maximize the SNR and simultaneously fit to the NIRCam aperture photometry[27]. We multiply the shape of the spectrum by a second-order polynomial, sampling over the polynomial coefficients in the fit. This essentially allows the NIRCam photometry to set the normalization of the spectrum while also correcting wavelength-dependent slit losses in the spectral calibration. The fits and associated parameter constraints are shown in Extended Data Figs. 2 and 3. We note that SED fitting is performed in the companion paper[27], yet there they fit only to NIRCam photometry, fixing the redshift to the spectroscopic redshift. Here we perform a complimentary analysis, fitting only to the spectra (except for JADES-GS-z13-0, as explained above).

For our BEAGLE fits, we mask the region of possible Lyα in JADES-GS-z10-0 (between 1.4148 μm and 1.4509 μm, inclusive), as it is offset from the break, and would require specialized modelling of the line shape and offset to be accounted for properly. The masked region is shown as pale blue in the spectrum in Extended Data Fig. 2 (top right) For JADES-GS-z12-0, we mask regions of rest-frame UV emission lines (light blue regions in Extended Data Fig. 2, bottom panel, covering 2.1081 μm to 2.1620 μm, 2.2875 μm to 2.3181 μm, and 2.6261 μm to 2.6533 μm) as noise structure in the spectrum is overfitted if left unmasked.

We then fit the spectra following the procedure of ref. [51]. We use a constant star formation history and fixed nebular parameters as we see no emission lines. The list of parameters employed in the fits, as well as chosen priors are given in Extended Data Table 2. We use the updated Bruzual and Charlot stellar population synthesis templates[52], as described in ref. [53], with the physically consistent nebular line + continuum emission grid of ref. [54]. We adopt a Chabrier[55] initial mass function with an upper mass limit of 100 $M_\odot$. We have verified that the results are not significantly changed when assuming an upper mass limit of 300 $M_\odot$. We account for the depletion of metals onto dust grains in the photoionized interiors of stellar birth clouds and include attenuation by dust in the outer neutral envelopes of the clouds and in the diffuse interstellar medium[56]. We set the ionization parameter, $\log U_s$, to depend on the nebular metallicity (and hence stellar metallicity) according to:

$$\log U_s = -3.638 + 0.055Z + 0.68Z^2$$

which follows the observations of ref. [57]. The results do not change significantly for JADES-GS-z10-0 and JADES-GS-z11-0 when $\log U_s$ is allowed to vary freely in the range $-4 < \log U_s < -1$. However, Z and $\log U_s$ are unconstrained in JADES-GS-z13-0, and poorly constrained in JADES-GS-z12-0, when $\log U_s$ is allowed to vary freely.

To test what is driving the fits to very low metallicity, we fit fixing the metallicity to intermediate values (between solar and 10% of solar). In this range, large [O II] $\lambda\lambda3,726, 3,729$ model fluxes are not described well by the data, and the derived constraints are pushed to low or high metallicities in the two lowest-redshift sources. We note, however, that reasonable intermediate metallicity solutions can be fit to the two higher-redshift galaxies. Moreover, letting $\log U_s$ vary freely in this metallicity range decreases model [O II] $\lambda\lambda3,726, 3,729$ fluxes but increases the model C III] $\lambda\lambda1,907, 1,909$ fluxes, constraining the fits still to the edges of the prior for the two lowest-redshift galaxies. It is a complex interplay in the limiting fluxes of these emission lines that drive the low-metallicity constraints in these galaxies.

As the constraints on the stellar metallicity are driven by the lack of strong emission lines, we tested whether recent cessation of star formation would change the constraints. We therefore tested a constant star formation history where the star formation rate of the recent 10 Myr was allowed to vary independently (and decrease). We find that the star formation rate, Ψ, is fairly unconstrained with low posterior median values, meaning recent cessation is consistent with the data. However, we still infer very low metallicities in JADES-GS-z10-0 and JADES-GS-z11-0 (the two with highest SNR spectra). For the two lower SNR spectra (JADES-GS-z12-0 and JADES-GS-z13-0), Z, $\hat\tau_v$ and Ψ are very poorly constrained when this extra free parameter is included. We show the results for JADES-GS-z10-0 and JADES-GS-z11-0 in Extended Data Table 3.

Another possibility to explain relatively weak line emission is a high escape of Lyman-continuum photons from the galaxy. We fit with a picket fence model (allowing for clear sight lines to the stars through the outer neutral envelopes of birth clouds[58]). The results are also given in Extended Data Table 3 for the two objects (JADES-GS-z10-0 and JADES-GS-z11-0) with the highest SNR spectra. We note that JADES-GS-z10-0 shows a solution with very low age (a few million years) and high escape fraction. The measured metallicity is marginally higher in this case, but still very low within the 1σ credible interval. JADES-GS-z11-0 does not show such a peak in the posterior distribution function, with fits still favouring older ages and escape fractions that span the input uniform prior. We note that these results are consistent with ref. [27], which finds similarly low age and high escape fraction for JADES-GS-z10-0 compared with JADES-GS-z11-0.

We also fit the spectra assuming the main feature is a Balmer break (see also 'Empirical measurements'). The results are shown in Extended Data Fig. 4. Here, we fit a delayed star formation history, which halted a billion-year prior to observation, varying metallicity, maximum stellar age and redshift within a tight prior centred on the assumed redshift in the case that the break is a Balmer break. We see that the fits consistently fail to reproduce the peak and blue slope redwards of the break, showing poor spectral fits. In addition, JADES-GS-z10-0 and JADES-GS-z11-0 show flux bluewards of the break in the fitted models, which is clearly inconsistent with the measured flux and noise limits.

We further explored possible low-redshift solutions to the photometry by SED fitting with BEAGLE-AGN[59], which includes narrow-line emission from obscured active galactic nuclei (AGN). This type of template is rarely used when fitting to high-redshift galaxy candidates. Three of the four galaxies provide intermediate redshift ($z \approx 3-3.5$) solutions to the photometry, and the fit to JADES-GS-z13-0 is shown in Extended Data Fig. 5. We see no strong emission lines in the spectra themselves, hence disproving these low-redshift possibilities allowed by the photometry.

Damping-wing profile

Galaxies at the very large redshifts presented in this paper are embedded in a largely neutral IGM, which has not yet undergone reionization. In this case, the effective optical depth of the hydrogen at lower redshifts along the line of sight becomes so large that the accumulated absorption in the Lorentzian scattering wing of the Lyα resonance

line causes intergalactic absorption to spill over into wavelengths above the rest-frame Lyα line. This so-called damping-wing absorption softens the sharp cut-off in the spectrum due to the intervening intergalactic hydrogen.

We have included the effect of the damping-wing absorption in our spectral fits using the prescription presented by Miralda-Escudé[60], who first pointed out the important effect. The model assumes that the damping wing arises in a uniformly distributed completely neutral IGM containing the bulk of the baryons in the universe. For a source at a given redshift z_s, it has only two free parameters, τ_0, the overall strength of the Lyα absorption in the form of the optical depth of the classical Gunn–Peterson trough[61] at a reference redshift of $z = 5$, and z_n, the redshift below which the intergalactic hydrogen is assumed to abruptly transition from fully neutral to fully ionized.

These two parameters are in turn set by the assumed cosmological model, which we here take to be Planck 2015 Λ cold dark matter model (where Λ is the cosmological constant)[62]. This model's baryonic density parameter of $\Omega_b h = 0.033$, total mass density parameter $\Omega_M = 0.309$, together with the primordial helium abundance of $Y = 24\%$ translate into $\tau_0 = 3.1 \times 10^5$. The Planck satellite also measured $z_n = 8.8$ for this cosmology, although the predicted damping-wing absorption is insensitive to this parameter at the large $z > 10$ redshifts relevant here. A partially reionized IGM is included in the customary manner by multiplying τ_0 by the volume-averaged neutral fraction x_{HI}. This simple model ignores the potential complications of the galaxies being observed displaying strong intrinsic neutral hydrogen absorption, or their having already reionized a large volume of their immediate surroundings[63].

In fitting the damping wing to JADES-GS-z11-0, we found a bimodality in the redshift solution, with a higher-redshift solution being consistent with a fully ionized IGM. We find that the final solution is quite sensitive to the adopted intrinsic underlying spectrum. We find solutions at higher redshifts provide poorer fits to the break region itself (shown in Extended Data Fig. 6 for completeness). The difference between fits was based on the definition of 'best fit' to the full spectrum used to fix physical parameters (either the minimum chi-2 solution, Fig. 3, or the maximum a posteriori probability solution shown here), while if we do not model Lyα emission in the fitting, we find a bimodal solution with redshift.

Data availability

The data that support the findings of this study are available from the corresponding authors upon reasonable request.

Code availability

BEAGLE is available via a Docker image (distributed through docker hub) upon request at https:/iap.fr/beagle.

References

1. Dayal, P. & Ferrara, A. Early galaxy formation and its large-scale effects. *Phys. Rep.* **780**, 1–64 (2018).
2. Bromm, V., Coppi, P. S. & Larson, R. B. The formation of the first stars. I. The primordial star-forming cloud. *Astrophys. J.* **564**, 23–51 (2002).
3. Schneider, R., Ferrara, A. & Salvaterra, R. Dust formation in very massive primordial supernovae. *Mon. Not. R. Astron. Soc.* **351**, 1379–1386 (2004).
4. Jeon, M., Bromm, V., Pawlik, A. H. & Milosavljević, M. The first galaxies: simulating their feedback-regulated assembly. *Mon. Not. R. Astron. Soc.* **452**, 1152–1170 (2015).
5. Vogelsberger, M. et al. High-redshift JWST predictions from IllustrisTNG: dust modelling and galaxy luminosity functions. *Mon. Not. R. Astron. Soc.* **492**, 5167–5201 (2020).
6. Hutter, A. et al. Astraeus I: the interplay between galaxy formation and reionization. *Mon. Not. R. Astron. Soc.* **503**, 3698–3723 (2021).
7. Wilkins, S. M. et al. First Light And Reionisation Epoch Simulations (FLARES) V: the redshift frontier. *Mon. Not. R. Astron. Soc.* **519**, 3118–3128 (2023).
8. Steidel, C. C., Giavalisco, M., Pettini, M., Dickinson, M. & Adelberger, K. L. Spectroscopic confirmation of a population of normal star-forming galaxies at redshifts z > 3. *Astrophys. J. Lett.* **462**, 17 (1996).
9. Madau, P. et al. High-redshift galaxies in the Hubble Deep Field: colour selection and star formation history to z~4. *Mon. Not. R. Astron. Soc.* **283**, 1388–1404 (1996).
10. Steidel, C. C. et al. Lyman break galaxies at redshift z ~3: survey description and full data set. *Astrophys. J.* **592**, 728–754 (2003).
11. Zavala, J. A. et al. A dusty starburst masquerading as an ultra-high redshift galaxy in JWST CEERS observations. *Astrophys. J. Lett.* **943**, L9 (2023).
12. Williams, H. et al. A highly magnified and extremely compact galaxy at redshift 9.51 with strong nebular emission. Preprint at https://arxiv.org/abs/2210.15699 (2022).
13. Oesch, P. A. et al. A remarkably luminous galaxy at z=11.1 measured with Hubble Space Telescope grism spectroscopy. *Astrophys. J.* **819**, 129 (2016).
14. Jiang, L. et al. Evidence for GN-z11 as a luminous galaxy at redshift 10.957. *Nat. Astron.* **5**, 256–261 (2021).
15. Donnan, C. T. et al. The evolution of the galaxy UV luminosity function at redshifts z ~8–15 from deep JWST and ground-based near-infrared imaging. *Mon. Not. R. Astron. Soc.* **518**, 6011–6040 (2023).
16. Harikane, Y. et al. A search for H-dropout Lyman break galaxies at z 12–16. *Astrophys. J.* **929**, 1 (2022).
17. Adams, N. J. et al. Discovery and properties of ultra-high redshift galaxies (9 < z < 12) in the JWST ERO SMACS 0723 field. *Mon. Not. R. Astron. Soc.* **518**, 4755–4766 (2023).
18. Finkelstein, S. L. et al. CEERS Key Paper I: An Early Look into the First 500 Myr of Galaxy Formation with JWST. Preprint at https://arxiv.org/abs/2211.05792 (2022).
19. Finkelstein, S. L. et al. A long time ago in a galaxy far, far away: a candidate z ~12 galaxy in early JWST CEERS imaging. *Astrophys. J. Lett.* **940**, L55 (2022).
20. Castellano, M. et al. Early results from GLASS-JWST. III. Galaxy candidates at z 9–15. *Astrophys. J. Lett.* **938**, 15 (2022).
21. Whitler, L. et al. On the ages of bright galaxies ~500 Myr after the Big Bang: insights into star formation activity at z≳15 with JWST. *Mon. Not. R. Astron. Soc.* **519**, 157–171 (2023).
22. Atek, H. et al. Revealing galaxy candidates out to z ~ 16 with JWST observations of the lensing cluster SMACS0723. *Mon. Not. R. Astron. Soc.* **519**, 1201–1220 (2023).
23. Bouwens, R. J. et al. Evolution of the UV LF from z~15 to z~8 using new JWST NIRCam medium-band observations over the HUDF/XDF. Preprint at https://arxiv.org/abs/2211.02607 (2022).
24. Bouwens, R. J. et al. UV luminosity density results at z>8 from the first JWST/NIRCam fields: limitations of early data sets and the need for spectroscopy. Preprint at https://arxiv.org/abs/2212.06683 (2022).
25. Jakobsen, P. et al. The Near-Infrared Spectrograph (NIRSpec) on the James Webb Space Telescope. I. Overview of the instrument and its capabilities. *Astron. Astrophys.* **661**, 80 (2022).
26. Rieke, M. J., Kelly, D. & Horner, S. Overview of James Webb Space Telescope and NIRCam's role. *Proc. SPIE* **5904**, 590401 (2005).
27. Robertson, B. E. et al. Identification and properties of intense star-forming galaxies at redshifts z > 10. *Nat. Astron.* https://doi.org/10.1038/s41550-023-01921-1 (2023).
28. Furtak, L. J. et al. JWST UNCOVER: a triply imaged faint quasar candidate at $z_{phot} \simeq 7.7$ Preprint at https://arxiv.org/abs/2212.10531 (2022).

29. Bouwens, R. J. et al. A candidate redshift z≈10 galaxy and rapid changes in that population at an age of 500 Myr. *Nature* **469**, 504–507 (2011).

30. Ellis, R. S. et al. The abundance of star-forming galaxies in the redshift range 8.5–12: new results from the 2012 Hubble Ultra Deep Field Campaign. *Astrophys. J. Lett.* **763**, 7 (2013).

31. Koekemoer, A. M. et al. The 2012 Hubble Ultra Deep Field (UDF12): observational overview. *Astrophys. J. Suppl. Ser.* **209**, 3 (2013).

32. Brammer, G. B. et al. A tentative detection of an emission line at 1.6 μm for the z ~12 candidate UDFj-39546284. *Astrophys. J. Lett.* **765**, 2 (2013).

33. Senchyna, P. et al. Ultraviolet spectra of extreme nearby star-forming regions—approaching a local reference sample for JWST. *Mon. Not. R. Astron. Soc.* **472**, 2608–2632 (2017).

34. Senchyna, P. et al. Extremely metal-poor galaxies with HST/COS: laboratories for models of low-metallicity massive stars and high-redshift galaxies. *Mon. Not. R. Astron. Soc.* **488**, 3492–3506 (2019).

35. Nanayakkara, T. et al. Exploring He II λ1640 emission line properties at z ~2-4. *Astron. Astrophys.* **624**, 89 (2019).

36. Reddy, N. A. et al. The MOSDEF Survey: significant evolution in the rest-frame optical emission line equivalent widths of star-forming galaxies at z = 1.4–3.8. *Astrophys. J.* **869**, 92 (2018).

37. Chevallard, J. & Charlot, S. Modelling and interpreting spectral energy distributions of galaxies with BEAGLE. *Mon. Not. R. Astron. Soc.* **462**, 1415–1443 (2016).

38. Hirashita, H., Il'in, V. B., Pagani, L. & Lefèvre, C. Evolution of dust porosity through coagulation and shattering in the interstellar medium. *Mon. Not. R. Astron. Soc.* **502**, 15–31 (2021).

39. Chevallard, J. et al. Physical properties and H-ionizing-photon production rates of extreme nearby star-forming regions. *Mon. Not. R. Astron. Soc.* **479**, 3264–3273 (2018).

40. Cullen, F. et al. The ultraviolet continuum slopes (β) of galaxies at z≈8–15 from JWST and ground-based near-infrared imaging. *Mon. Not. R. Astron. Soc.* **520**, 14–23 (2023).

41. Topping, M. W. et al. Searching for extremely blue UV continuum slopes at z = 7–11 in JWST/NIRCam imaging: implications for stellar metallicity and ionizing photon escape in early galaxies. *Astrophys. J.* **941**, 153 (2022).

42. Bouwens, R. J. et al. Very blue UV-continuum slope β of low luminosity z ~7 galaxies from WFC3/IR: evidence for extremely low metallicities? *Astrophys. J. Lett.* **708**, 69–73 (2010).

43. Greig, B. et al. IGM damping wing constraints on reionization from covariance reconstruction of two z ≳ 7 QSOs. *Mon. Not. R. Astron. Soc.* **512**, 5390–5403 (2022).

44. Davies, F. B. et al. Predicting quasar continua near Lyα with principal component analysis. *Astrophys. J.* **864**, 143 (2018).

45. Ferruit, P. et al. The Near-Infrared Spectrograph (NIRSpec) on the James Webb Space Telescope. II. Multi-object spectroscopy (MOS). *Astron. Astrophys.* **661**, 81 (2022).

46. Birkmann, S. M. et al. Wavelength calibration of the JWST near-infrared spectrograph (NIRSpec). *Proc. SPIE* **8150**, 81500 (2011).

47. Böker, T. et al. The spectro-photometric calibration of the JWST NIRSpec instrument. *Proc. SPIE* **8442**, 84423 (2012).

48. Giardino, G. et al. The impact of cosmic rays on the sensitivity of JWST/NIRSpec. *Publ. Astron. Soc. Pac.* **131**, 094503 (2019).

49. Kriek, M. et al. Direct measurements of the stellar continua and Balmer/4000 Å breaks of red z > 2 galaxies: redshifts and improved constraints on stellar populations. *Astrophys. J.* **645**, 44–54 (2006).

50. Calzetti, D., Kinney, A. L. & Storchi-Bergmann, T. Dust extinction of the stellar continua in starburst galaxies: the ultraviolet and optical extinction law. *Astrophys. J.* **429**, 582 (1994).

51. Chevallard, J. et al. Simulating and interpreting deep observations in the Hubble Ultra Deep Field with the JWST/NIRSpec low-resolution 'prism'. *Mon. Not. R. Astron. Soc.* **483**, 2621–2640 (2019).

52. Bruzual, G. & Charlot, S. Stellar population synthesis at the resolution of 2003. *Mon. Not. R. Astron. Soc.* **344**, 1000–1028 (2003).

53. Vidal-García, A., Charlot, S., Bruzual, G. & Hubeny, I. Modelling ultraviolet-line diagnostics of stars, the ionized and the neutral interstellar medium in star-forming galaxies. *Mon. Not. R. Astron. Soc.* **470**, 3532–3556 (2017).

54. Gutkin, J., Charlot, S. & Bruzual, G. Modelling the nebular emission from primeval to present-day star-forming galaxies. *Mon. Not. R. Astron. Soc.* **462**, 1757–1774 (2016).

55. Chabrier, G. Galactic stellar and substellar initial mass function. *Publ. Astron. Soc. Pac.* **115**, 763–795 (2003).

56. Charlot, S. & Fall, S. M. A simple model for the absorption of starlight by dust in galaxies. *Astrophys. J.* **539**, 718–731 (2000).

57. Carton, D. et al. Inferring gas-phase metallicity gradients of galaxies at the seeing limit: a forward modelling approach. *Mon. Not. R. Astron. Soc.* **468**, 2140–2163 (2017).

58. Heckman, T. M. et al. Extreme feedback and the epoch of reionization: clues in the local universe. *Astrophys. J.* **730**, 5 (2011).

59. Vidal-García, A. et al. BEAGLE-AGN I: simultaneous constraints on the properties of gas in star-forming and AGN narrow-line regions in galaxies. Preprint at https://arxiv.org/abs/2211.13648 (2022).

60. Miralda-Escude, J. Reionization of the intergalactic medium and the damping wing of the Gunn–Peterson trough. *Astrophys. J.* **501**, 15–22 (1998).

61. Gunn, J. E. & Peterson, B. A. On the density of neutral hydrogen in inter-galactic space. *Astrophys. J.* **142**, 1633–1636 (1965).

62. Planck Collaboration Planck 2015 results. XIII. Cosmological parameters. *Astron. Astrophys.* **594**, 13 (2016).

63. McQuinn, M., Lidz, A., Zaldarriaga, M., Hernquist, L. & Dutta, S. Probing the neutral fraction of the IGM with GRBs during the epoch of reionization. *Mon. Not. R. Astron. Soc.* **388**, 1101–1110 (2008).

64. Endsley, R. et al. A JWST/NIRCam study of key contributors to reionization: the star-forming and ionizing properties of UV-faint z ~ 7–8 galaxies. Preprint at https://arxiv.org/abs/2208.14999 (2022).

Acknowledgements

Author contributions

Competing interests

The authors declare no competing interests.

Additional information

Correspondence and requests for materials should be addressed to Emma Curtis-Lake or Stefano Carniani.

Peer review information *Nature Astronomy* thanks the anonymous reviewer(s) for their contribution to the peer review of this work.

Reprints and permissions information is available at www.nature.com/reprints.

Publisher's note Springer Nature remains neutral with regard to jurisdictional claims in published maps and institutional affiliations.

Emma Curtis-Lake [1] ✉, **Stefano Carniani** [2,33] ✉, **Alex Cameron** [3], **Stephane Charlot** [4], **Peter Jakobsen** [5,6], **Roberto Maiolino** [7,8,9], **Andrew Bunker** [3], **Joris Witstok** [7,8], **Renske Smit** [10], **Jacopo Chevallard** [3], **Chris Willott** [11], **Pierre Ferruit** [12], **Santiago Arribas** [13], **Nina Bonaventura** [5,6], **Mirko Curti** [7,8], **Francesco D'Eugenio** [7,8], **Marijn Franx** [14], **Giovanna Giardino** [15], **Tobias J. Looser** [7,8], **Nora Lützgendorf** [16], **Michael V. Maseda** [17], **Tim Rawle** [16], **Hans-Walter Rix** [18], **Bruno Rodríguez del Pino** [13], **Hannah Übler** [7,8], **Marco Sirianni** [16], **Alan Dressler** [19], **Eiichi Egami** [20], **Daniel J. Eisenstein** [21], **Ryan Endsley** [22], **Kevin Hainline** [20], **Ryan Hausen** [23], **Benjamin D. Johnson** [21], **Marcia Rieke** [20], **Brant Robertson** [24], **Irene Shivaei** [20], **Daniel P. Stark** [20], **Sandro Tacchella** [7,8], **Christina C. Williams** [25], **Christopher N. A. Willmer** [20], **Rachana Bhatawdekar** [26], **Rebecca Bowler** [27], **Kristan Boyett** [28,29], **Zuyi Chen** [20], **Anna de Graaff** [18], **Jakob M. Helton** [20], **Raphael E. Hviding** [20], **Gareth C. Jones** [3], **Nimisha Kumari** [30], **Jianwei Lyu** [20], **Erica Nelson** [31], **Michele Perna** [13], **Lester Sandles** [7,8], **Aayush Saxena** [3,9], **Katherine A. Suess** [24,32], **Fengwu Sun** [20], **Michael W. Topping** [20], **Imaan E. B. Wallace** [3] & **Lily Whitler** [20]

[1]Centre for Astrophysics Research, Department of Physics, Astronomy and Mathematics, University of Hertfordshire, Hatfield, UK. [2]Scuola Normale Superiore, Pisa, Italy. [3]Department of Physics, University of Oxford, Oxford, UK. [4]Sorbonne Université, CNRS, UMR 7095, Institut d'Astrophysique de Paris, Paris, France. [5]Cosmic Dawn Center (DAWN), Copenhagen, Denmark. [6]Niels Bohr Institute, University of Copenhagen, Copenhagen, Denmark. [7]Kavli Institute for Cosmology, University of Cambridge, Cambridge, UK. [8]Cavendish Laboratory - Astrophysics Group, University of Cambridge, Cambridge, UK. [9]Department of Physics and Astronomy, University College London, London, UK. [10]Astrophysics Research Institute, Liverpool John Moores University, Liverpool, UK. [11]NRC Herzberg, Victoria, British Columbia, Canada. [12]European Space Agency, European Space Astronomy Centre, Madrid, Spain. [13]Centro de Astrobiología (CAB), CSIC–INTA, Madrid, Spain. [14]Leiden Observatory, Leiden University, Leiden, The Netherlands. [15]ATG Europe for the European Space Agency, ESTEC, Noordwijk, The Netherlands. [16]European Space Agency (ESA), ESA Office, STScI, Baltimore, MD, USA. [17]Department of Astronomy, University of Wisconsin-Madison, Madison, WI, USA. [18]Max-Planck-Institut für Astronomie, Heidelberg, Germany. [19]The Observatories of the

Carnegie Institution for Science, Pasadena, CA, USA. [20]Steward Observatory University of Arizona, Tucson, AZ, USA. [21]Center for Astrophysics, Harvard & Smithsonian, Cambridge, MA, USA. [22]Department of Astronomy, University of Texas, Austin, TX, USA. [23]Department of Physics and Astronomy, The Johns Hopkins University, Baltimore, MD, USA. [24]Department of Astronomy and Astrophysics University of California, Santa Cruz, CA, USA. [25]NSF's National Optical-Infrared Astronomy Research Laboratory, Tucson, AZ, USA. [26]European Space Agency, ESA/ESTEC, Noordwijk, NL, The Netherlands. [27]Jodrell Bank Centre for Astrophysics, Department of Physics and Astronomy, School of Natural Sciences, The University of Manchester, Manchester, UK. [28]School of Physics, University of Melbourne, Parkville, Victoria, Australia. [29]ARC Centre of Excellence for All Sky Astrophysics in 3 Dimensions (ASTRO 3D), Canberra, Australian Capital Territory, Australia. [30]AURA for European Space Agency, Space Telescope Science Institute, Baltimore, MD, USA. [31]Department for Astrophysical and Planetary Science, University of Colorado, Boulder, CO, USA. [32]Kavli Institute for Particle Astrophysics and Cosmology and Department of Physics, Stanford University, Stanford, CA, USA. [33]These authors contributed equally: Emma Curtis-Lake, Stefano Carniani. ✉e-mail: e.curtis-lake@herts.ac.uk; stefano.carniani@sns.it
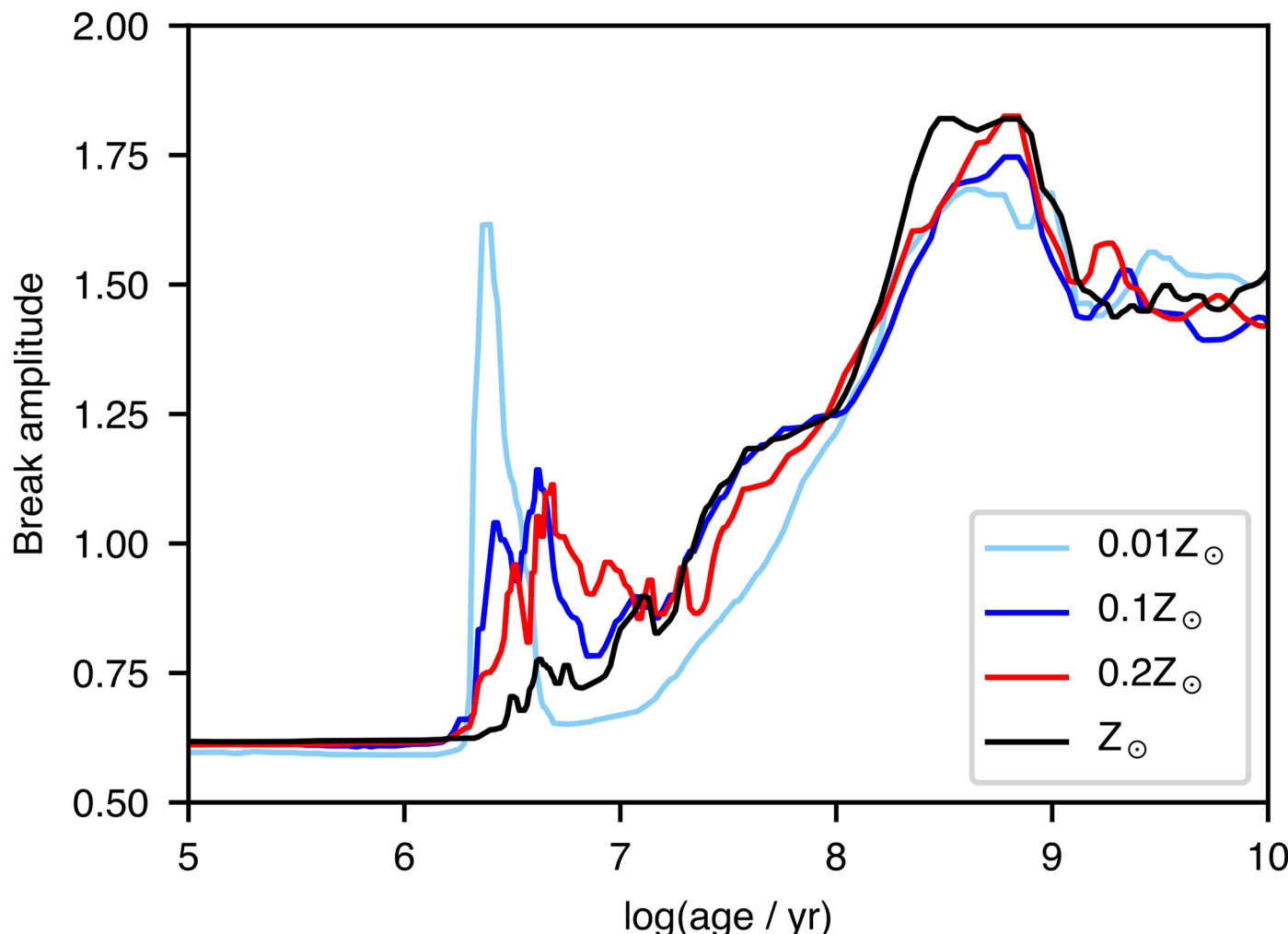
Extended Data Fig. 1 | Model Balmer break strength. Balmer break amplitude plotted against age for single stellar populations with metallicities $0.01Z_{\odot}$, $0.1Z_{\odot}$, $0.2Z_{\odot}$, and $Z_{\odot}$ (as indicated), according to the models described in Section 3. The break is defined as the ratio of the flux f_{λ} integrated over the rest-frame 3751–4198Å wavelength range to that in the rest-frame 3145–3563 Å wavelength range. The peak at early ages for all metallicities arises from the onset or red supergiant stars, and that around 6×10^8 yr from bright asymptotic-giant-branch stars.
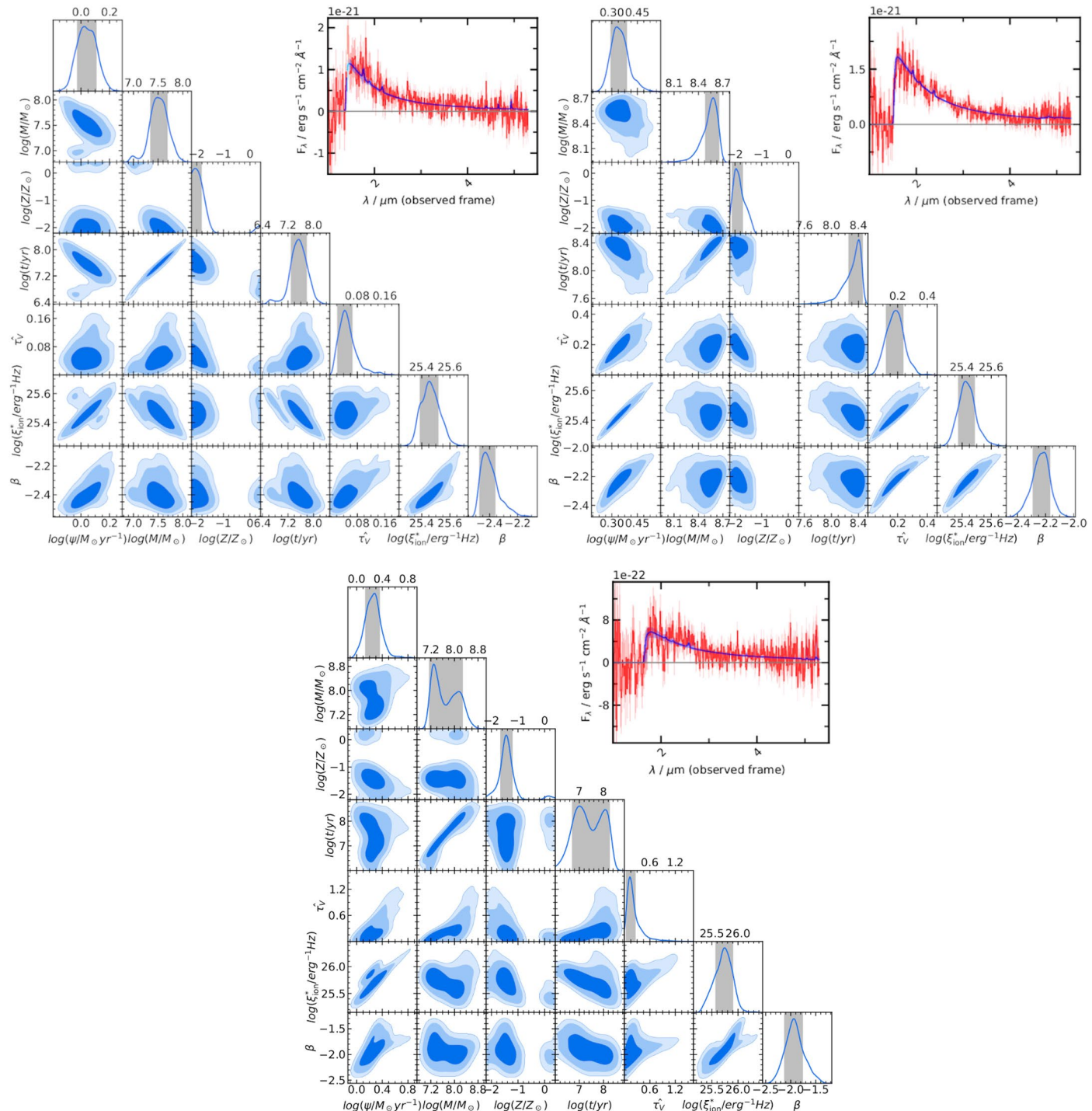
Extended Data Fig. 2 | BEAGLE fits to GS-z10-0, GS-z11-0 and GS-z12-0. The results of full spectral fitting to JADES-GS-z10-0 (top left), JADES-GS-z11-0 (top right) and JADES-GS-z12-0 (bottom) with BEAGLE. We fit models to spectra extracted over the full shutter aperture to minimise the wavelength-dependent losses due to varying point spread function (PSF). The triangle plot shows the 2D (off-diagonal) and 1D (along the main diagonal) posterior probability distributions on stellar mass (M), metallicity (Z), maximum age of stars (t) and the effective dust attenuation optical depth in the V-band ($\hat{\tau}_V$) which are all derived from the beagle fits. We also include the model constraints on the star formation rate (Ψ), UV slope (β) and ionizing photon emissivity (ξ_ion), which are derived parameters of the model. The dark, medium and light blue contours show the extents of the 1, 2 and 3σ credible regions of the posterior probability, respectively. The inset panel shows the observed spectrum and 1σ standard errors per pixel in red and light red respectively, and the median and 1σ range in fitted model spectra in blue. We fit with a constant star formation history (more details in the text and Methods section 3).
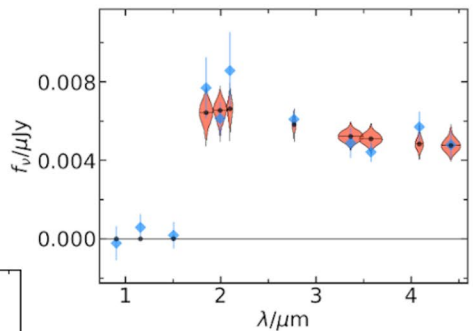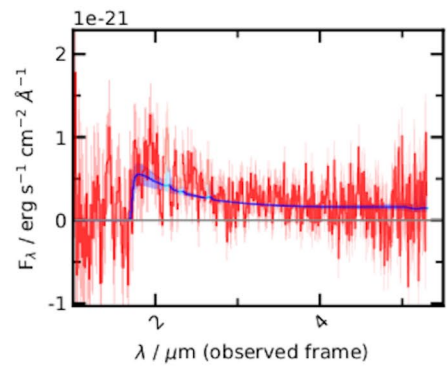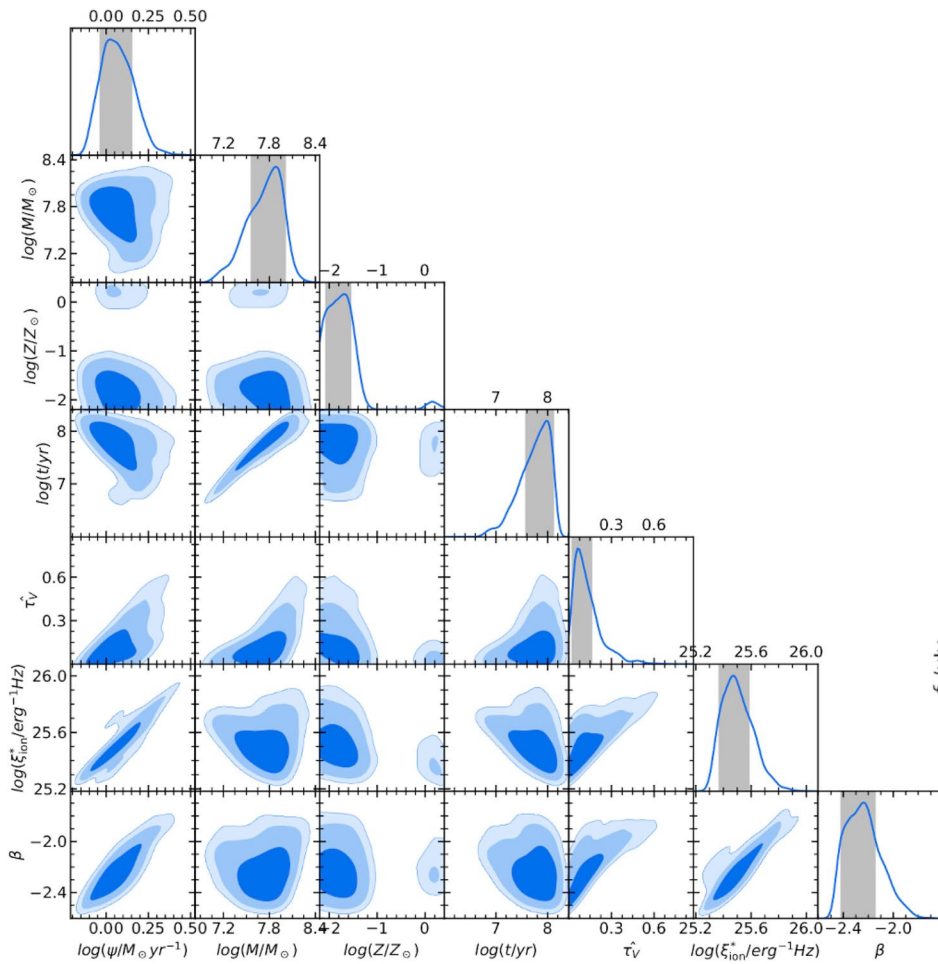
Extended Data Fig. 3 | BEAGLE fit to GS-z13-0. As for Extended Data Fig. 2, but for BEAGLE fits to JADES-GS-z13-0. The bottom right panel shows the observed photometry and associated as blue diamonds and associated 1σ s.d. error bars while the coral shaded regions show the model photometry in the same bands. Since this galaxy is very close to the edge of the shutter, we use an extraction over 3 pixels to maximize the S/N. Then to account for wavelength-dependent slit losses we simultaneously fit the spectrum and NIRCam photometry.
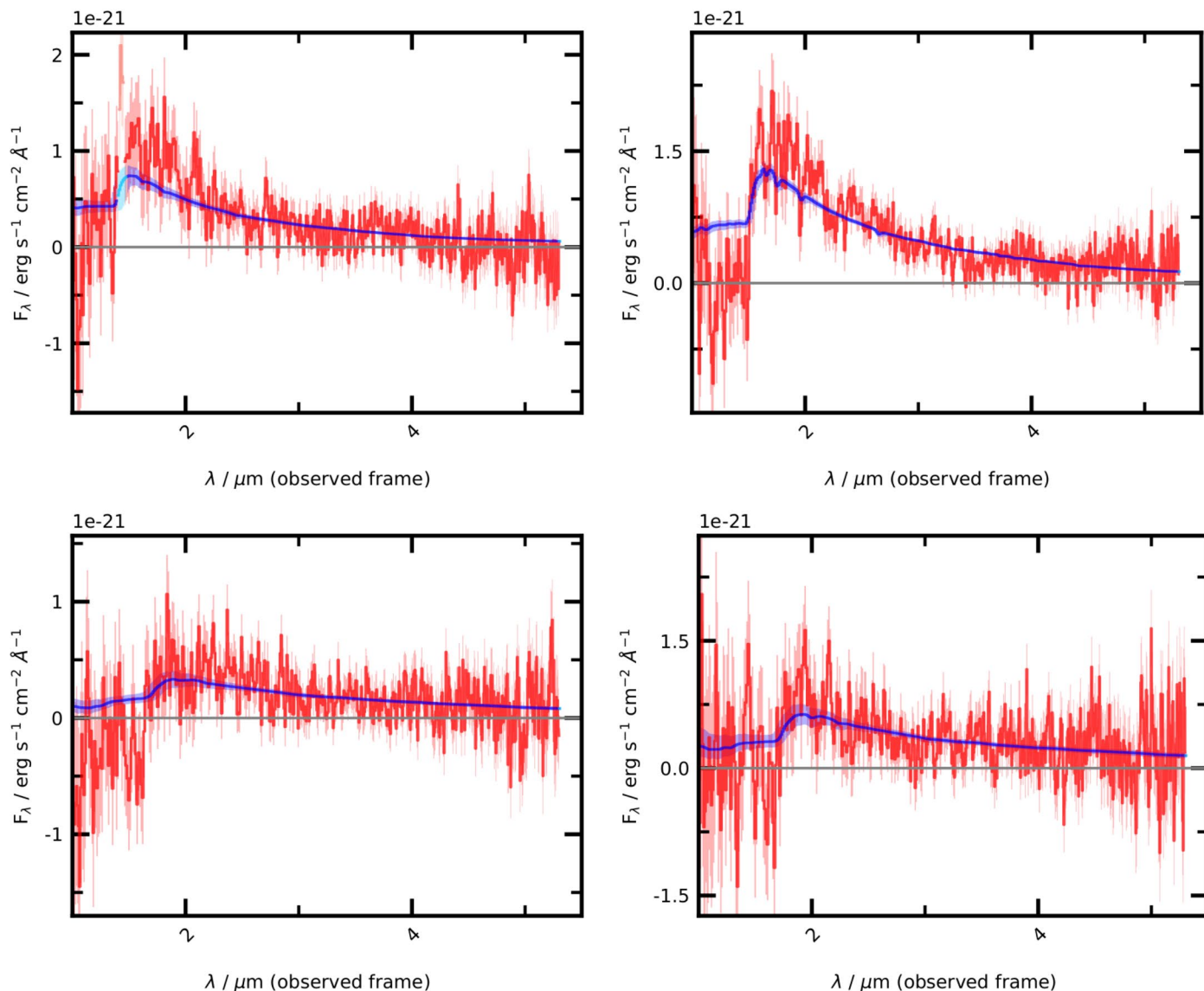
Extended Data Fig. 4 | Alternative balmer break fits to the spectra. The fitted spectra if we force the observed spectral break to be interpreted as a Balmer break rather than a Lyman break. We see that the fits fail to reproduce the blue slopes red-ward of the spectral break, and in the cases of JADES-GS-z10-0 and JADES-GS-z11-0, flux in the fitted models blue-ward of the break is notably higher than the observed flux. Combined with the limits placed in Methods section 2 (and presented in Table 1), these fits show that the observed spectra are inconsistent with being Balmer breaks. The panels show the observed spectrum and 1σ standard error per pixel in red and light red respectively, and the median and 1σ range in fitted model spectra in blue.
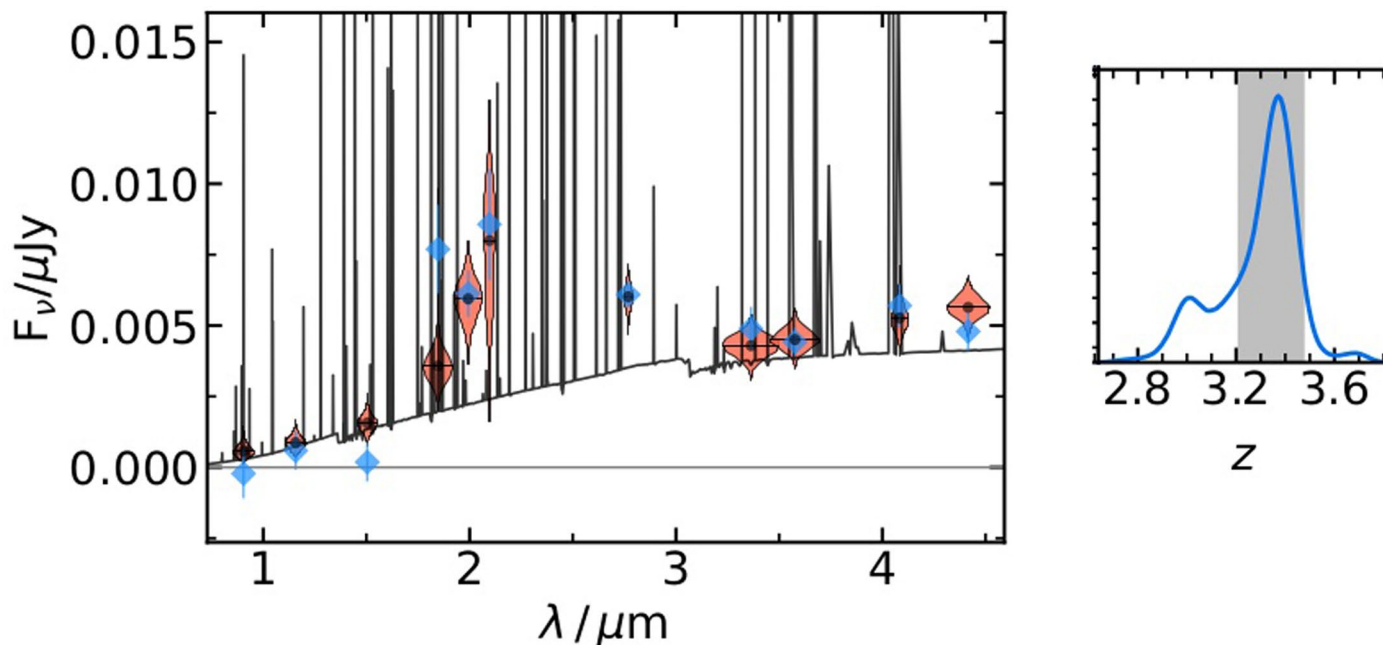
Extended Data Fig. 5 | Alternative redshift solution to GS-z13-0. The left panel shows the measured NIRCam photometry and associated 1σ s.d. error bars for JADES-GS-z13-0 as blue diamonds and lines, respectively. The coral violin shaded regions show the underlying model values. The black line shows the maximum a posteriori probability solution with strong emission lines due to active-galactic-nuclei narrow-line emission. The right panel shows a zoom of the intermediate redshift solution fitted to the photometry.
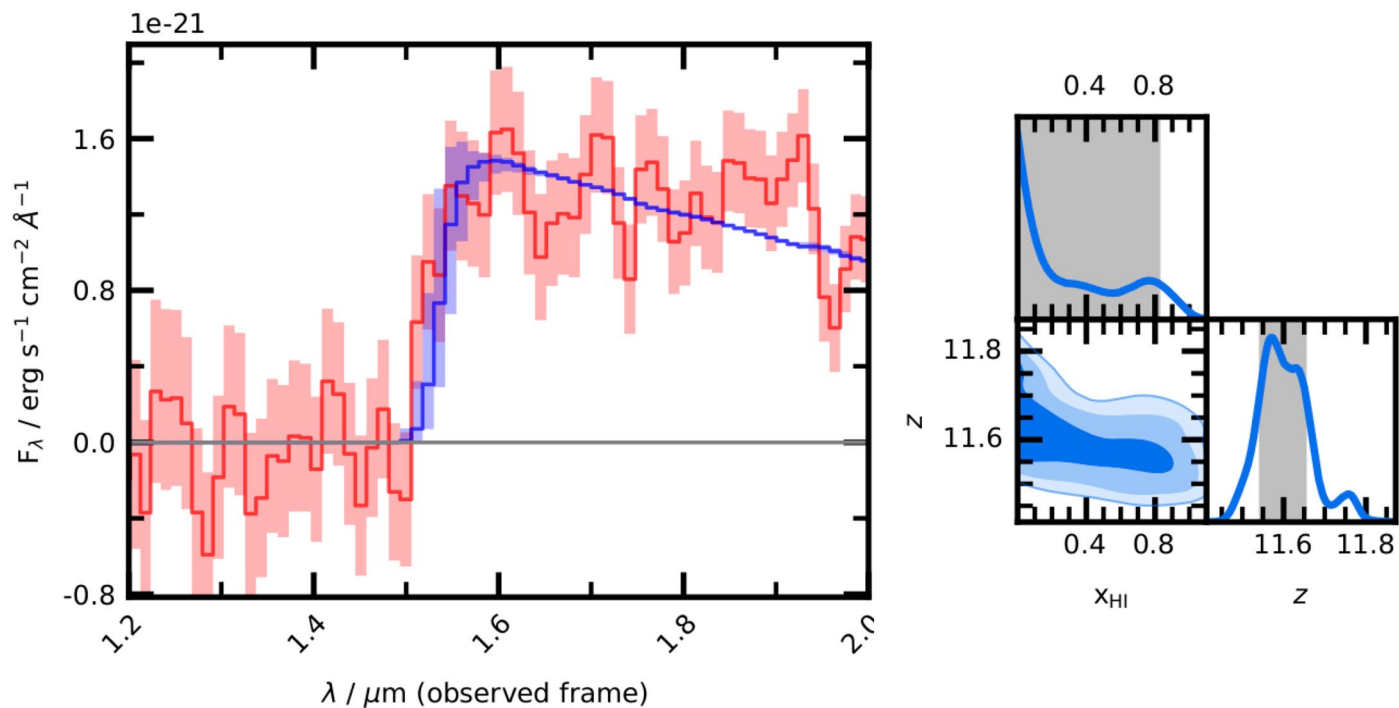
Extended Data Fig. 6 | Higher-redshift damping-wing fit to GS-z13-0. As for Fig. 3 but showing a fit to the damping wing using a different definition of 'best fit' to fix the physical parameters of the galaxy spectrum which pushes the constraints to a higher-redshift solution.

Extended Data Table 1 | Emission-line limiting fluxes

JADES-ID:	GS-z10-0	GS-z11-0	GS-z12-0	GS-z13-0
EW(C III]$\lambda\lambda$1907, 1909)	< 13.74	< 5.84	< 11.94	< 14.40
EW(He IIλ1640)	< 14.80	< 5.98	< 12.84	< 14.52
EW(C IVλ1548)	< 13.92	< 6.08	< 12.98	< 14.20
EW(O III]$\lambda\lambda$1661,1666)	< 14.12	< 5.94	< 12.80	< 14.74
EW([O II]$\lambda\lambda$3726,3729)	< 28.10	< 9.07	< 16.62	< 16.82
C III]$\lambda\lambda$1907,1909	< 8.43e-20	< 5.60e-20	< 4.88e-20	< 7.09e-20
He IIλ1640	< 1.26e-19	< 8.08e-20	< 7.14e-20	< 1.01e-19
C IV$\lambda\lambda$1548,1550	< 1.33e-19	< 9.23e-20	< 7.98e-20	< 1.11e-19
O III]$\lambda\lambda$1661,1666	< 1.17e-19	< 7.77e-20	< 6.92e-20	< 9.93e-20
[O II] $\lambda\lambda$3726,3729	< 2.99e-20	< 2.86e-20	< 5.09e-20	< 5.29e-20

2σ upper limits on the rest-frame equivalent widths (in Å) and observed line fluxes (in erg s^{-1}cm^{-2}) of rest-frame UV emission lines.

Extended Data Table. 2 | BEAGLE parameters

Parameter	Description	Prior
$\log(M_{tot}/M_\odot)$	Logarithm of the integrated SFH.	Uniform $\in [6, 12]$
$M/M_\odot$	Stellar mass, including stellar remnants.	Not fitted (dependent on M_{tot}, Z and t)
$\psi/M_\odot yr^{-1}$	Current star formation rate.	Not fitted (dependent on M_{tot} and t)
$\log(Z/Z_\odot)$	Logarithm of metallicity of stars.	Uniform $\in [-2.2, 0.4]$
$\log(Z_{gas}^{HII}/Z_\odot)$	Metallicity of gas in H ii regions.	Set equal to Z
$\hat{\tau}_v$	Total V -band attenuation optical depth in the interstellar medium (ISM).	Exponential $\in [0, 6]$
μ	Fraction of $\hat{\tau}_v$ arising from dust in the diffuse ISM	Fixed to 0.4.
$\log U_s$	Effective gas ionization parameter in H ii regions	Dependent on Z_{gas}^{HII} (following Eq. 1)
ξ_d	Dust-to-metal mass ratio in H ii regions.	Fixed to 0.1
n_H/cm^{-3}	Hydrogen gas density in H ii regions.	Fixed to 100.
$(C/O)/(C/O_\odot)$	Carbon-to-oxygen abundance ratio in units of $(C/O)_\odot = 0.44$	Fixed to unity.
$m_{up}/M_\odot$	Upper mass cutoff of the IMF	Fixed to 100.
$\log(t/Gyr)$	Logarithm of the age of the oldest stars.	Uniform $\in [6, 10.8]$
z	redshift	Gaussian $\mu_z = z_{1216}$, $\sigma_z = 0.01$

Parameter descriptions and prior distributions used in BEAGLE fitting.

Extended Data Table 3 | Exploring different parameter constraints with BEAGLE

	JADES-GS-z10-0		*JADES-GS-z11-0*	
	SFR_{10} varied	f_{esc} varied	SFR_{10} varied	f_{esc} varied
$log(M/M_\odot)$	$7.8^{+0.12}_{-0.11}$	$7.41^{+0.1}_{-0.11}$	$8.85^{+0.12}_{-0.15}$	$8.70^{+0.11}_{-0.16}$
$\psi/M_\odot yr^{-1}$	$-2.11^{+1.28}_{-1.34}$	$2.43^{+0.65}_{-0.58}$	$-1.87^{+1.45}_{-1.37}$	$2.83^{+0.76}_{-0.47}$
$log(t/yr)$	$7.15^{+0.17}_{-0.11}$	$6.29^{+0.19}_{-0.2}$	$8.12^{+0.20}_{-0.28}$	$8.26^{+0.14}_{-0.23}$
$log(Z/Z_\odot)$	$-1.88^{+0.36}_{-0.21}$	$-1.7^{+0.41}_{-0.33}$	$-1.87^{+0.33}_{-0.21}$	$-1.8^{+0.29}_{-0.25}$
$\widehat{\tau}_v$	$0.3^{+0.26}_{-0.18}$	$0.09^{+0.05}_{-0.04}$	$0.68^{+0.18}_{-0.2}$	$0.26^{+0.1}_{-0.08}$
ξ_{ion}	$25.04^{+0.17}_{-0.21}$	$26.01^{+0.12}_{-0.13}$	$24.73^{+0.25}_{-0.15}$	$25.54^{+0.12}_{-0.08}$
f_{esc}	–	$0.86^{+0.1}_{-0.13}$	–	$0.64^{+0.24}_{-0.32}$

BEAGLE-derived parameters when additionally fitting the star formation rate in the last 10 Myr allowed to vary freely independently of the previous history (labelled SFR_{10} varied), or when varying the escape fraction of Lyman-continuum f_{esc} (labelled f_{esc} varied). We show the results when fitting to the two objects with highest S/N, JADES-GS-z10-0 and JADES-GS-z11-0 because the constraints on the other two objects are very poor when adding an extra free parameter to the fits.